Spin-torque-induced excitations of in-phase oscillation in an in-plane-magnetized elliptical nanopillar device: A numerical study

Kiwamu Kudo,* Tazumi Nagasawa, Hirofumi Suto, Rie Sato, and Koichi Mizushima
Corporate Research and Development Center, Toshiba Corporation, 1, Komukai-Toshiba-cho, Saiwai-ku, Kawasaki 212-8582, Japan
(Received 23 December 2009; revised manuscript received 11 June 2010; published 25 June 2010)

According to the analytic theory of spin-torque-induced magnetization oscillations, it is expected that single-mode states involving a spatially uniform oscillation can emerge when the sign of the nonlinear frequency-shift coefficient is positive. For an in-plane-magnetized elliptical nanopillar device, the sign can be positive when the in-plane bias field is applied along the direction far from the in-plane easy axis. By using micromagnetic simulations, we demonstrate that the in-phase oscillation, in which all the magnetic moments in the free layer oscillate in phase, emerges in the elliptical nanopillar device under the bias field in the direction far from the in-plane easy axis. The consistency between the theory and the simulations indicates that the magnetization-oscillation patterns excited in the elliptical device are mainly determined by the cooperative effect between two factors: the exchange spin-wave dispersion and the nonlinear shift of local frequencies.

DOI: 10.1103/PhysRevB.81.224432 PACS number(s): 75.78.Cd, 85.70.Kh, 05.45.−a

I. INTRODUCTION

Since the demonstration of the microwave magnetization precession due to the spin-torque effect in a magnetic-layered nanostructure,[1,2] the research and development of the novel nanosized oscillator—the spin-torque oscillator (STO)—has been very active in the field of magnetic devices.[3,4] There are two typical geometries of STOs: magnetic nanocontact and nanopillar geometries. Depending on the geometries and the orientations of the applied magnetic field, various types of magnetization-oscillation modes are excited in the "free" layer. In an in-plane-magnetized nanocontact, the self-localized spin-wave "bullet" or/and the propagating linear spin-wave mode is excited depending on the applied field angle. These modes, which are initially predicted by the theories[5,6] and confirmed by the micromagnetic simulations,[7,8] have recently been observed in an experiment.[9] In the case of magnetic nanopillars, a greater variety of oscillation modes has been observed in experiments and obtained by micromagnetic simulations: the center and ends' oscillation modes in the elliptical element,[10] the coherent oscillations in the elliptical nanopillar device under the bias magnetic field along the hard axis,[11,12] the chaotic oscillation behavior in the square nanopillar structures,[13] and so on.

According to the theory based on the spin-wave Hamiltonian formalism, the Landau-Lifshitz-Gilbert-Slonczewski (LLGS) equation for the spin-torque-induced magnetization oscillation near the threshold reduces to the form of the complex Ginzburg-Landau equation (CGLE).[6,14] The CGLE provides a universal description of slow spatiotemporal variation near a supercritical Hopf bifurcation and has been used to describe a huge variety of phenomena.[15] The equation has the following form:

$$\frac{\partial W}{\partial t} = W + (1 + ic_1)\nabla^2 W - (1 - ic_3)|W|^2 W. \tag{1}$$

The expression (1) for the spin-torque-induced magnetization oscillation is obtained by a suitable scale transformation of Eq. (3.30) of Ref. 14. The complex amplitude $W(\boldsymbol{r},t)$ represents the amplitude and phase of the lowest temporal Fourier mode of the magnetization oscillations. The parameter c_1 represents the dispersion coefficient for the exchange spin waves normalized by the magnitude of the diffusion. The parameter c_3 represents the normalized nonlinear frequency-shift coefficient and has various values depending on magnetic anisotropies and an external magnetic field.[14,16–20] In a nondissipative limit ($|c_{1,3}| \to \infty$), the CGLE reduces to the nonlinear Schrödinger equation (NLSE).

For an infinitely large system, the CGLE (1) has the plane-wave solutions involving a uniform-oscillation solution that can be interpreted as synchronized states in an oscillatory medium[21] but the solutions are unstable in the parameter range of $1 - c_1 c_3 < 0$ (the Benjamin-Feir unstable range), and turbulence appears.[15] The term 1 appearing in this instability condition implies the effect of stabilizing a uniform oscillation by the diffusion term $1 \cdot \nabla^2 W$. On the other hand, the term $c_1 c_3$ implies the cooperative effect between the two factors: the exchange spin-wave dispersion represented by $ic_1\nabla^2 W$ and the amplitude-dependent shift of local frequencies represented by $ic_3|W|^2 W$. Since the parameter c_1 is large and negative in the spin-torque-induced excitation system,[6,22] the instability condition reduces to

$$|c_1| c_3 \lesssim 0. \tag{2}$$

This condition signifies that the synchronized states, or the single-mode states characterized by a single wave number, are permitted to emerge when the coefficient of the nonlinear frequency shift is positive ($c_3 > 0$). On the other hand, when the coefficient of the nonlinear frequency shift is negative ($c_3 < 0$), the frequency nonlinearity and the spin-wave dispersion cooperatively lead to the repulsive interaction between the magnetic moments, and the instability occurs.

For the nanocontact structures, the theory based on the CGLE or the perturbed NLSE has been used to analyze the oscillation modes,[6,7,9,14,22] showing that Eq. (2) is the necessary condition for the existence of the self-localized spin-wave bullet in a nanocontact geometry. In the case of the in-plane-magnetized, *isotropic*, free layer, the coefficient of

 ©2010 The American Physical Society

frequency shift is negative ($c_3<0$) so that the self-localized spin-wave bullet can be supported. In the case of normally magnetized nanocontact, the coefficient of frequency shift is positive ($c_3>0$) so that the propagating linear spin-wave mode can emerge.[22] The mode transition between the spin-wave bullet and the propagating linear spin wave is caused by the change in the sign of the nonlinear frequency-shift coefficient.[22]

In contrast to the nanocontact structures, the theory based on the CGLE has not been employed explicitly to examine the oscillation modes for the pillar structures. In this study, we consider the magnetization dynamics in an in-plane-magnetized, *anisotropic*, pillar structure. In particular, an in-plane-magnetized, elliptical nanopillar device with the shape anisotropy is considered. For the in-plane-magnetized, anisotropic film, the sign of the nonlinear frequency-shift coefficient can change from negative to positive as the in-plane bias field is rotated from the in-plane easy axis to the hard axis under the condition that the bias field H_0 satisfies $H_u<H_0<4H_u$, where H_u is the *effective* in-plane anisotropy field.[17,20] Accordingly, from the theory based on the CGLE, it is expected that the oscillation-mode transition due to the sign change in the nonlinear frequency-shift coefficient occurs in the in-plane-magnetized, anisotropic film depending on the in-plane bias-field angle ϕ_0. In addition, some synchronized states involving a uniform oscillation are expected to emerge under the in-plane bias field in the direction far from the in-plane easy axis. In a uniform oscillation, all the magnetic moments in the free layer oscillate in phase with the same amplitudes. Such a homogeneous oscillation mode is probably useful for the oscillator application.

Motivated by the theoretical consideration, we have performed the micromagnetic simulations for the variation in magnetization dynamics with the in-plane bias-field angle ϕ_0 focusing on the emergence of a uniform oscillation. It is demonstrated that the in-phase oscillation, in which all the magnetic moments in the free layer oscillate in phase, emerges in the elliptical nanopillar device under the in-plane bias field in the direction far from the in-plane easy axis.

This paper is organized in the following way. In Sec. II, we derive again the CGLE from the LLGS equation by the reduction method, which was applied to a reaction-diffusion equation in the earlier study,[23] in order to clarify the correspondence between the theory and the simulations (see, for example, Sec. II B), although the CGLE for the spin-torque-induced excitations is well known.[6,14] In Sec. III, we present details of the micromagnetic simulations. A spatial two-dimensional (2D) "minimal" micromagnetic simulation is performed, i.e., only zero-temperature magnetization dynamics of a 2D thin film is considered. The simulations are performed on an infinitely large film (Sec. III B) as well as an elliptical device (Sec. III C). The simulation for the infinite film is used to mediate between the simulation for the elliptical device and the theory based on the CGLE. In Sec. III C, the magnetization-oscillation patterns excited in the elliptical device are discussed by comparing them with those excited in the infinite film. It is demonstrated that the mode transition from incoherent to in-phase oscillation occurs owing to the sign change in the nonlinear frequency-shift coefficient. In Sec. IV, we conclude the paper.

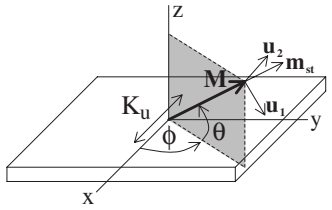

FIG. 1. 2D magnetic thin film extending in the x-y plane. The unit vectors $\hat{\boldsymbol{u}}_1$, $\hat{\boldsymbol{u}}_2$, and $\boldsymbol{m}_{st}$ form an orthonormal right-handed system: $\hat{\boldsymbol{u}}_1 \equiv \sin\theta\cos\phi\,\hat{\boldsymbol{x}}+\sin\theta\sin\phi\,\hat{\boldsymbol{y}}-\cos\hat{\boldsymbol{z}}$, $\hat{\boldsymbol{u}}_2 \equiv -\sin\phi\,\hat{\boldsymbol{x}}+\cos\phi\,\hat{\boldsymbol{y}}$, and $\boldsymbol{m}_{st} \equiv \cos\theta\cos\phi\,\hat{\boldsymbol{x}}+\cos\theta\sin\phi\,\hat{\boldsymbol{y}}+\sin\theta\hat{\boldsymbol{z}}$. The vector $\boldsymbol{m}_{st}$ denotes the uniform steady solution of Eq. (3).

II. COMPLEX GINZBURG-LANDAU EQUATION

A. Derivation of the CGLE

To derive the CGLE, we expand the LLGS equation around the uniform steady solution up to the third-order terms. The expanded LLGS equation has the form of a reaction-diffusion equation. Once the reaction-diffusion equation is obtained, the reduction method,[23–25] just as it is, is applicable to the expanded equation.

We consider the 2D magnetic film extending in the x-y plane. The easy-axis magnetic anisotropy $K_u(>0)$ lies in the film along the x direction as shown in Fig. 1. It is assumed that the film thickness is less than the exchange length $l_{ex}=\sqrt{A/2\pi M_s^2}$, where A is the exchange stiffness constant and M_s is the saturation magnetization. It is supposed that the film is so large that the effect of boundaries is negligible.

The LLGS equation for the free-layer magnetization vector $\boldsymbol{m}(\boldsymbol{r},t)=\boldsymbol{M}(\boldsymbol{r},t)/M_s$ $[\boldsymbol{r}=(x,y)]$ is given by

$$\frac{\partial \boldsymbol{m}}{\partial t} = -\gamma \boldsymbol{m}\times\boldsymbol{H}_{\text{eff}} + \alpha \boldsymbol{m}\times\frac{\partial \boldsymbol{m}}{\partial t} + \sigma I \boldsymbol{m}\times(\boldsymbol{m}\times\boldsymbol{p}), \quad (3)$$

where γ is the gyromagnetic ratio and α is the Gilbert damping constant. The value of α is assumed to be ~ 0.01, which is typical for soft magnetic materials. The first term of the right-hand side of Eq. (3) is the torque forcing the magnetization vector to precess around the effective magnetic field $\boldsymbol{H}_{\text{eff}}$. We assume that the effective magnetic field is given by

$$\boldsymbol{H}_{\text{eff}}[\boldsymbol{m}] = \boldsymbol{H}_0 - H_{\text{dem}}(\boldsymbol{m}\cdot\hat{\boldsymbol{z}})\hat{\boldsymbol{z}} + H_u(\boldsymbol{m}\cdot\hat{\boldsymbol{x}})\hat{\boldsymbol{x}} + \boldsymbol{H}_{\text{ex}}, \quad (4)$$

where $\boldsymbol{H}_0$ is the external bias field, H_{dem} is the demagnetizing field, H_u is the in-plane anisotropy field given by $H_u=2K_u/M_s$, and $\boldsymbol{H}_{\text{ex}}$ is the inhomogeneous exchange field given by $\boldsymbol{H}_{\text{ex}}=4\pi M_s l_{\text{ex}}^2\nabla^2\boldsymbol{m}$. The second term of the right-hand side of Eq. (3) represents the relaxation of the magnetization vector to the steady state. The third term of the right-hand side of Eq. (3) is the Slonczewski spin-torque term[26] in which σ is the spin-transfer efficiency, I is the direct current, and $\boldsymbol{p}=p_x\hat{\boldsymbol{x}}+p_y\hat{\boldsymbol{y}}+p_z\hat{\boldsymbol{z}}$ is the pinned-layer magnetization vector with the unit length. The efficiency σ is given by $\sigma=\epsilon g\mu_B/(2|e|M_sV_{\text{free}})$, where ϵ is the spin-polarization factor, g is the Landé factor, μ_B is the Bohr magneton, e is the electron charge, and V_{free} is the volume of the free layer.

The LLGS Eq. (3) has a uniform steady solution $\boldsymbol{m}_{st}$, which satisfies $\partial\boldsymbol{m}_{st}/\partial t=0$ with $\boldsymbol{H}_{\text{ex}}=0$. The steady solution is defined as $\boldsymbol{m}_{st}\equiv\cos\theta\cos\phi\,\hat{\boldsymbol{x}}+\cos\theta\sin\phi\,\hat{\boldsymbol{y}}+\sin\theta\,\hat{\boldsymbol{z}}$,

where (θ,ϕ) is the spherical coordinate shown in Fig. 1. The direction (θ,ϕ) is determined by solving the following equation:

$$\boldsymbol{H}_{\mathrm{eff}}[\boldsymbol{m}_{\mathrm{st}}] - \frac{\sigma I}{\gamma'}\boldsymbol{m}_{\mathrm{st}} \times \boldsymbol{p} = H\boldsymbol{m}_{\mathrm{st}}, \tag{5}$$

where H is the auxiliary field and $\gamma' \equiv \gamma/(1+\alpha^2)$. Note that the vector $\boldsymbol{m}_{\mathrm{st}}$, and thus the angles (θ,ϕ) and the field H, depend on current, i.e., $\boldsymbol{m}_{\mathrm{st}}=\boldsymbol{m}_{\mathrm{st}}(I)$. In the absence of current $(I=0)$, the solution of Eq. (5) coincides with the equilibrium vector $\boldsymbol{m}_{\mathrm{eq}}$. The equilibrium vector is determined by

$$\boldsymbol{H}_{\mathrm{eff}}[\boldsymbol{m}_{\mathrm{eq}}] = H\boldsymbol{m}_{\mathrm{eq}}. \tag{6}$$

In the case of an in-plane-magnetized film under an in-plane bias field $\boldsymbol{H}_0=H_0(\cos\phi_0,\sin\phi_0,0)$, for example, the equilibrium angle θ_{eq} is equal to zero $(\theta_{\mathrm{eq}}=0)$, and the equilibrium angle ϕ_{eq} is determined by solving the following equations:

$$\begin{cases} H\cos\phi_{\mathrm{eq}} = H_0\cos\phi_0 + H_{\mathrm{u}}\cos\phi_{\mathrm{eq}} \\ H\sin\phi_{\mathrm{eq}} = H_0\sin\phi_0. \end{cases} \tag{7}$$

In addition to the steady-solution vector $\boldsymbol{m}_{\mathrm{st}}$, the two unit vectors $\hat{\boldsymbol{u}}_1$ and $\hat{\boldsymbol{u}}_2$ forming an orthonormal right-handed system are introduced (see Fig. 1). By the bases, the magnetization vector around the steady solution is expressed by $\boldsymbol{m}(\boldsymbol{r},t)=u_1(\boldsymbol{r},t)\hat{\boldsymbol{u}}_1+u_2(\boldsymbol{r},t)\hat{\boldsymbol{u}}_2+u_3(\boldsymbol{r},t)\boldsymbol{m}_{\mathrm{st}}$ with $|u_{1,2}|\ll 1$ and $u_3\simeq 1$. Since the LLGS Eq. (3) preserves the norm of $|\boldsymbol{m}|=1$, only two components of the magnetization vector are independent. For the sake of convenience, the pinned-layer magnetization vector $\boldsymbol{p}$ is also expressed by the bases as $\boldsymbol{p}=p_1\hat{\boldsymbol{u}}_1+p_2\hat{\boldsymbol{u}}_2+p_3\boldsymbol{m}_{\mathrm{st}}$. The component p_3 can be written as $p_3=\boldsymbol{m}_{\mathrm{st}}\cdot\boldsymbol{p}=\cos\beta$, where β is the angle between $\boldsymbol{m}_{\mathrm{st}}$ and $\boldsymbol{p}$.

By the Taylor expansion of the LLGS equation around the uniform steady solution up to the third order, we obtain the following equation in terms of the deviations $\boldsymbol{u}(\boldsymbol{r},t) \equiv [u_1(\boldsymbol{r},t),u_2(\boldsymbol{r},t)]^{\mathrm{T}}$:

$$\frac{\partial \boldsymbol{u}}{\partial t} = (L + D\nabla^2)\boldsymbol{u} + M\boldsymbol{uu} + N\boldsymbol{uuu}, \tag{8}$$

where $M\boldsymbol{uu}$ and $N\boldsymbol{uuu}$ denote the second- and third-order expansion terms with the dyadic and triadic notations, respectively. This equation has the form of a reaction-diffusion equation. To obtain Eq. (8), the spatial variation in $u_i(\boldsymbol{r},t)$ $(i=1,2)$ has been assumed to be small, and the nonlinear terms including spatial variations such as $u_i\nabla^2 u_j$ have been neglected. In Eq. (8), the linear coefficient matrix L is given by

$$L = \begin{pmatrix} \sigma I\cos\beta - (\omega_3+\alpha\omega_2) & -\omega_1 - \alpha(\omega_3+\sigma I\cos\beta) \\ \omega_2 - \alpha(\omega_3 - \sigma I\cos\beta) & \sigma I\cos\beta + (\omega_3 - \alpha\omega_1) \end{pmatrix}, \tag{9}$$

where

$$\omega_1/\gamma' \equiv H - H_{\mathrm{u}}\sin^2\phi,$$

$$\omega_2/\gamma' \equiv H + H_{\mathrm{dem}}\cos^2\theta - H_{\mathrm{u}}\sin^2\theta\cos^2\phi,$$

$$\omega_3/\gamma' \equiv H_{\mathrm{u}}\sin\theta\sin\phi\cos\phi, \tag{10}$$

and the diffusion matrix D is given by

$$D = \gamma' 4\pi M_{\mathrm{s}} l_{\mathrm{ex}}^2 \begin{pmatrix} \alpha & 1 \\ -1 & \alpha \end{pmatrix}. \tag{11}$$

Note that the matrix L is the function of the current I, i.e., $L=L(I)$. In particular, β and ω_i $(i=1,2,3)$ in the matrix L depend on the current implicitly. The stability of the steady solution is determined by the eigenvalues of L. The eigenvalues of $L(I)$ are given by

$$\lambda_{\pm}(I) = \tau(I) \pm \sqrt{\tau^2(I) - \delta(I)}, \tag{12}$$

where

$$\tau(I) \equiv \frac{1}{2}\mathrm{tr}L(I) = \sigma I\cos\beta - \frac{\alpha}{2}(\omega_1+\omega_2) \tag{13}$$

and

$$\delta(I) \equiv \det L(I) = (1+\alpha^2)[\omega_1\omega_2 - \omega_3^2 + (\sigma I\cos\beta)^2]. \tag{14}$$

For the excitation of magnetization oscillations, it is necessary that the matrix L has a pair of complex-conjugate eigenvalues, i.e., $\tau^2(I)<\delta(I)$. In this case, whether the steady solution $\boldsymbol{m}_{\mathrm{st}}(I)$ is stable or not is determined by the sign of the real part of the eigenvalues, $\tau(I)$. The solution is asymptotically stable for $\tau(I)<0$. On the other hand, the solution is unstable for $\tau(I)>0$ and an oscillation emerges. The oscillation threshold current I_{c} is determined by the equation $\tau(I_{\mathrm{c}})=0$, i.e.,

$$\sigma I_{\mathrm{c}}\cos\beta_{\mathrm{c}} = \frac{\alpha}{2}(\omega_1+\omega_2), \tag{15}$$

where β_{c} is the angle between $\boldsymbol{m}_{\mathrm{st}}(I_{\mathrm{c}})$ and $\boldsymbol{p}$. We consider the case that $\tau(I)<0$ for $0\le I<I_{\mathrm{c}}$ and $\tau(I)>0$ for $I>I_{\mathrm{c}}$. In this case, the steady solution $\boldsymbol{m}_{\mathrm{st}}(I)$ is stable for $0\le I<I_{\mathrm{c}}$, and the oscillatory instability occurs at $I=I_{\mathrm{c}}$ (Hopf bifurcation). The condition that $\tau(I=0)<0$, i.e., $\omega_1+\omega_2>0$, signifies that the equilibrium vector corresponds to the minimum magnetic energy state, which is relevant in the absence of the current.

In the following, we restrict our attention to the current region near the threshold. Accordingly, the expansion of the LLGS equation is executed around the vector $\boldsymbol{m}_{\mathrm{st}}(I_{\mathrm{c}})$. The vector $\boldsymbol{m}_{\mathrm{st}}(I_{\mathrm{c}})$ denotes the oscillation-center point. We ignore the implicit higher-order dependence of β and ω_i $(i=1,2,3)$ on the current I and replace it with I_{c}. Moreover, we ignore the terms of $\mathcal{O}(\alpha^2)$. Thus, the eigenvalue of L is written as

$$\lambda_{\pm}(I) = \pm i\omega_0 + \mu\sigma I_{\mathrm{c}}\cos\beta_{\mathrm{c}}, \tag{16}$$

where $\mu=(I-I_{\mathrm{c}})/I_{\mathrm{c}}$ measures the distance from the threshold I_{c}, and $\omega_0=\sqrt{\det L(I_{\mathrm{c}})}\simeq\sqrt{\omega_1\omega_2-\omega_3^2}$ corresponds to the ferromagnetic resonance frequency at the threshold. In the expression of the eigenvalue, $\lambda_+(I)=i\omega_0+\mu\sigma I_{\mathrm{c}}\cos\beta_{\mathrm{c}}$, the term $i\omega_0$ represents the critical part and the term $\mu\sigma I_{\mathrm{c}}\cos\beta_{\mathrm{c}}$ represents the remaining part. The matrix L is correspondingly divided into the two parts such that $L=L_0+\mu L_1$, where the

matrix L_0 is the critical part given by $L_0=L(I_c)$ and the matrix L_1 is the remaining part given by $L_1=\sigma I_c \cos\beta_c \mathbf{1}$ ($\mathbf{1}$ is the unit matrix). Accordingly, Eq. (8) is rewritten as

$$\left(\frac{\partial}{\partial t}-L_0\right)\boldsymbol{u}=\mu L_1\boldsymbol{u}+D\nabla^2\boldsymbol{u}+M\boldsymbol{uu}+N\boldsymbol{uuu}. \tag{17}$$

Although the nonlinear terms $M\boldsymbol{uu}$ and $N\boldsymbol{uuu}$ generally depend on the current I, the current appearing in those terms is replaced by I_c to give $M_0\boldsymbol{uu}$ and $N_0\boldsymbol{uuu}$. Now, the application of the reduction method described in detail in the textbooks[24,25] to Eq. (17) can be carried out in a direct way. All terms of the right-hand side of Eq. (17) are treated as perturbation terms in the reduction method. By the reduction in Eq. (17), the following 2D CGLE for the complex amplitude $W(x,y,t)$ is obtained:

$$\frac{\partial W}{\partial t}=\mu\lambda_1 W-g|W|^2W+d\nabla^2 W. \tag{18}$$

The coefficients in Eq. (18) are given by

$$\lambda_1=(\boldsymbol{U}^*\cdot L_1\boldsymbol{U})=\sigma I_c\cos\beta_c, \tag{19}$$

$$d\equiv d'+id''=(\boldsymbol{U}^*\cdot D\boldsymbol{U})=\gamma 4\pi M_s l_{ex}^2\left(\alpha-i\frac{\omega_1+\omega_2}{2\omega_0}\right), \tag{20}$$

and

$$\begin{aligned} g\equiv g'+ig''=&-3(\boldsymbol{U}^*\cdot N_0\bar{\boldsymbol{U}}\boldsymbol{UU})+4(\boldsymbol{U}^*\cdot M_0\boldsymbol{U}L_0^{-1}M_0\boldsymbol{U}\bar{\boldsymbol{U}})\\ &+2[\boldsymbol{U}^*\cdot M_0\bar{\boldsymbol{U}}(L_0-2i\omega_0)^{-1}M_0\boldsymbol{UU}]. \end{aligned} \tag{21}$$

The vectors $\boldsymbol{U}$ and $\boldsymbol{U}^*$ appearing in Eqs. (19)–(21) are the right and left eigenvectors of L_0 corresponding to the eigenvalue $i\omega_0$, respectively. These vectors are normalized as $\boldsymbol{U}^*\boldsymbol{U}=\bar{\boldsymbol{U}}^*\boldsymbol{U}=1$, where $\bar{\boldsymbol{U}}$ denotes a complex conjugate of $\boldsymbol{U}$. Since the analytic expression for g [Eq. (21)] is rather complicated, the numerical calculation is necessary for obtaining the value. The complex amplitude $W(\boldsymbol{r},t)$ gives the amplitude and phase of the lowest temporal Fourier mode of magnetization oscillations, and the original variable $\boldsymbol{u}$ is given by $\boldsymbol{u}(\boldsymbol{r},t)=W(\boldsymbol{r},t)\boldsymbol{U}e^{i\omega_0 t}+\bar{W}(\boldsymbol{r},t)\bar{\boldsymbol{U}}e^{-i\omega_0 t}$. In Eq. (18), the linear term $\mu\lambda_1 W$ denotes the linear growth. The nonlinear terms of Eq. (18), $-g'|W|^2W$ and $-ig''|W|^2W$, represent the nonlinear relaxation and the nonlinear shift of frequencies, respectively. The linear spatial variation terms of Eq. (18), $d'\nabla^2 W$ and $id''\nabla^2 W$, represent the diffusion and the linear dispersion, respectively.

In the supercritical region ($\mu>0$) for $g'>0$, the scale transformation,

$$(\mu\lambda_1 t,\sqrt{\mu\lambda_1/d'}\boldsymbol{r},\sqrt{g'/\mu\lambda_1}W)\rightarrow(t,\boldsymbol{r},W), \tag{22}$$

gives a simpler form of Eq. (18),

$$\frac{\partial W}{\partial t}=W+(1+ic_1)\nabla^2 W-(1-ic_3)|W|^2W, \tag{23}$$

where

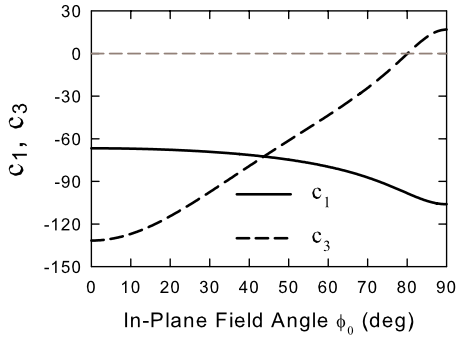

FIG. 2. (Color online) Dependence of the CGLE parameters, c_1 and c_3, on the in-plane field angle ϕ_0 in the in-plane magnetized magnetic film. The parameters chosen are $H_0=600$ Oe, $H_u=300$ Oe, $H_{dem}=7200$ Oe, $\alpha=0.025$, and $\boldsymbol{p}=\boldsymbol{m}_{eq}$.

$$c_1\equiv\frac{d''}{d'}=-\frac{\omega_1+\omega_2}{2\alpha\omega_0}\quad\text{and}\quad c_3\equiv-\frac{g''}{g'}. \tag{24}$$

This is the same form as Eq. (1). From the viewpoint of the CGLE (23) regarding the spin-torque-induced excitations, the collective dynamics of magnetic moments is determined by only the two parameters, c_1 and c_3. From Eq. (24), it is found that the parameter c_1 has a rather large negative value since the value of α is small ($\sim$0.01). Note that the values of c_1 and c_3 depend on the direction of the bias field via the direction of the oscillation-center point $\boldsymbol{m}_{st}(I_c)$.

As mentioned in the introduction (Sec. I), the form of Eq. (23) for the spin-torque-induced excitations has been obtained by Slavin *et al.* [see Eq. (3.30) of Ref. 14]. They have used the classical Hamiltonian formalism for spin waves to derive the form of Eq. (23). In contrast to their derivation method, our method is based on the reduction in a reaction-diffusion equation, and the similarity and the difference between the spin-torque-induced excitation system and the reaction-diffusion system is clear. For example, the form of the diffusion matrix D represented by Eq. (11) is peculiar to the spin-torque-induced excitation system. From Eq. (11), one can see that the antisymmetric part of the matrix D is much larger than the symmetric part. In contrast, the diffusion matrix usually has a small antisymmetric part in the reaction-diffusion system.[24] The large value of $|c_1|$ in the spin-torque-induced excitation system is caused by the large antisymmetric part of D.

B. CGLE parameters

Figure 2 shows the dependence of the parameters, c_1 and c_3, on the in-plane bias-field angle ϕ_0 in the in-plane-magnetized, anisotropic film. The values of c_1 and c_3 are calculated by Eq. (24). The parameters chosen are $H_0=600$ Oe, $H_u=300$ Oe, $H_{dem}=7200$ Oe, and $\alpha=0.025$, where H_0 is the magnitude of the in-plane bias field $\boldsymbol{H}_0=H_0(\cos\phi_0,\sin\phi_0,0)$. The pinned-layer magnetization vector is chosen as $\boldsymbol{p}=\boldsymbol{m}_{eq}=(\cos\phi_{eq},\sin\phi_{eq},0)$, where the angle ϕ_{eq} is determined by solving Eq. (7). When $\boldsymbol{p}=\boldsymbol{m}_{eq}$, the oscillation-center point $\boldsymbol{m}_{st}(I_c)$ coincides with the equilibrium vector $\boldsymbol{m}_{eq}$. From Fig. 2, one can see that the parameter c_1 has a large negative value. The parameter c_3 has a wide

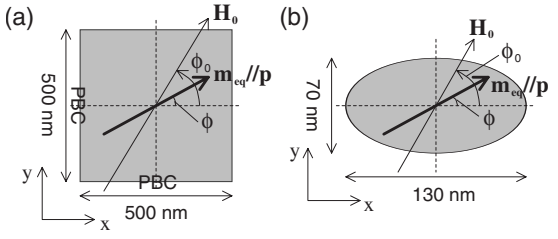

FIG. 3. In-plane-magnetized thin films on which the micromagnetic simulations are performed: (a) the infinite film and (b) the elliptical film.

range of values depending on the in-plane field angle ϕ_0 and changes the sign at $\phi_0 \sim 80°$. The sign of c_3 is positive when the bias field is rotated far from the in-plane easy axis ($\phi_0 \gtrsim 80°$ for the parameters used).

Although we have assumed that $\boldsymbol{p}=\boldsymbol{m}_{\rm eq}$, the angular dependence of c_1 and c_3 shown above hardly changes when the angle $\beta_{\rm eq}$ between $\boldsymbol{m}_{\rm eq}$ and $\boldsymbol{p}$ is less than $\sim 45°$, i.e., $|\tan \beta_{\rm eq}| \lesssim 1$. This can be understood as follows. From Eq. (15), at the threshold, the magnitude of the term $\sigma I \boldsymbol{m}_{\rm st} \times \boldsymbol{p}$ that appears in Eq. (5) is estimated as $|\sigma I_c \boldsymbol{m}_{\rm st} \times \boldsymbol{p}| = [\alpha(\omega_1+\omega_2)/2] \tan \beta_c$. Since the value of α is small (~ 0.01), the quantity $|\sigma I_c \boldsymbol{m}_{\rm st} \times \boldsymbol{p}|/\gamma'$ is much smaller than the magnitude of the effective magnetic field as long as $|\tan \beta_c| \lesssim 1$. Accordingly, if $|\tan \beta_c| \lesssim 1$, Eq. (5) is close to Eq. (6), and the oscillation-center point $\boldsymbol{m}_{\rm st}(I_c)$ approximately coincides with the equilibrium vector $\boldsymbol{m}_{\rm eq}$. Therefore, when the condition of $|\tan \beta_{\rm eq}| \lesssim 1$ is satisfied, the oscillation-center point $\boldsymbol{m}_{\rm st}(I_c)$, which determines the angular dependence of c_1 and c_3, approximately coincides with the equilibrium vector $\boldsymbol{m}_{\rm eq}$. Consequently, the values of c_1 and c_3 hardly change for the pinned-layer vector $\boldsymbol{p}$ in the range of $|\tan \beta_{\rm eq}| \lesssim 1$.

As shown in Fig. 2, in the in-plane magnetized film with the parameters of $H_0=600$ Oe, $H_{\rm u}=300$ Oe, $H_{\rm dem}=7200$ Oe, $\alpha=0.025$, and $\boldsymbol{p}=\boldsymbol{m}_{\rm eq}$, the sign of the normalized nonlinear frequency-shift coefficient c_3 changes from negative to positive at $\phi_0 \sim 80°$. Accordingly, from the theory based on the CGLE, it is expected that the oscillation-mode transition occurs at $\phi_0 \sim 80°$. In addition, some synchronized states are expected to emerge under the in-plane bias field in the direction far from the in-plane easy axis ($\phi_0 \gtrsim 80°$). We confirm these predictions by micromagnetic simulations in the next section.

III. MICROMAGNETIC SIMULATIONS

A. Simulation setup

We consider the in-plane magnetized film with the effective in-plane anisotropy field $H_{\rm u} \simeq 300$ Oe and the effective demagnetizing field $H_{\rm dem} \simeq 7200$ Oe. By applying the field $\boldsymbol{H}_0 = H_0(\cos \phi_0, \sin \phi_0, 0)$ ($H_0=600$ Oe) to the film, we examine the variation in magnetization dynamics with the in-plane field angle ϕ_0. Two kinds of magnetic films with the thickness of 4 nm are simulated: an infinitely large film and an elliptical film. The sketches of the two films are shown in Figs. 3(a) and 3(b). The magnetization-oscillation patterns excited in the elliptical film are discussed by comparing them with those excited in the infinite film. For the comparison between them, we use almost the same parameters for the two films.

Our simulation code is based on the integration of the LLGS equation. Only zero-temperature, 2D free-layer magnetization dynamics in the layered magnetic structure is considered. The effect of the pinned layer is taken into account just via the vector $\boldsymbol{p}$ included in the Slonczewski term. The other effects of the pinned layer (e.g., a stray field from the pinned to the free layer) are ignored. We integrate the LLGS equation by a fourth-order Runge-Kutta method with a fixed time step Δt. We use random initial conditions by generating uniform pseudorandom numbers. The calculation of the demagnetizing field, which involves a large computational cost, is performed by the fast Fourier transform (FFT) method.

For the simulation of the infinite film, we use the periodic boundary conditions and limit the computational region to $500 \times 500 \times 4$ nm^3 [Fig. 3(a)]. The computational region is discretized in a mesh of $(500/128) \times (500/128) \times 4$ nm^3 cells. The long-range dipole-dipole interaction between magnetization cells, which results in the demagnetizing field, is cut off at the length $l_{\rm cut}=2.5$ μm. No quantitative changes in simulation results are produced if $l_{\rm cut} \geq 2.5$ μm.

For the simulation of the elliptical film [Fig. 3(b)], we use the free boundary conditions $\partial \boldsymbol{m}/\partial n|_{\rm boundary}=0$ $(n=x,y,z)$. The computational region is discretized in a mesh of $2.5 \times 2.5 \times 4$ nm^3 cells. The zero-padding method is used to calculate the demagnetizing field, which makes the FFT of convolutions applicable to nonperiodic structures.[27]

The parameters used in the simulations for both the infinite film and the elliptical film are the exchange stiffness constant $A=1.3 \times 10^{-6}$ erg/cm, the Gilbert damping constant $\alpha=0.025$, the gyromagnetic ratio $\gamma=1.76 \times 10^7$ (Oe s)$^{-1}$, and the time step $\Delta t \simeq 14.2$ fs. The other parameters, the in-plane uniaxial anisotropy $K_{\rm u}$ and the saturation magnetization $M_{\rm s}$, are chosen as follows: $K_{\rm u}=8.6 \times 10^4$ erg/cm^3 and $M_{\rm s}=573$ emu/cm^3 for the infinite film, and $K_{\rm u}=0$ erg/cm^3 and $M_{\rm s}=650$ emu/cm^3 for the elliptical film. By drawing the field-magnetization curves numerically, we have checked that these parameters make the effective values $H_{\rm u} \simeq 300$ Oe and $H_{\rm dem} \simeq 7200$ Oe, respectively. Note that the effective anisotropy field $H_{\rm u}$ for the elliptical film is caused by the shape anisotropy.

In the formulation described in Sec. II, under the parameters of $\boldsymbol{H}_0 = H_0(\cos \phi_0, \sin \phi_0, 0)$ ($H_0=600$ Oe), $H_{\rm u}=300$ Oe, and $H_{\rm dem}=7200$ Oe, the equilibrium magnetization vector $\boldsymbol{m}_{\rm eq}$ lies in the film, and the in-plane angle $\phi_{\rm eq}$ is calculated by Eq. (7). By calculating the value of $\boldsymbol{m}_{\rm eq}$ for each ϕ_0, we set the direction of the pinned-layer magnetization vector as $\boldsymbol{p}=\boldsymbol{m}_{\rm eq}$. In this case, the steady-solution vector $\boldsymbol{m}_{\rm st}(I)$ coincides with the equilibrium vector $\boldsymbol{m}_{\rm eq}$, and the threshold current I_c is theoretically given by

$$\sigma I_c = \frac{\gamma \alpha}{2}(2H - H_{\rm u} \sin^2 \phi_{\rm eq} + H_{\rm dem}) \tag{25}$$

from Eq. (15). By calculating the value of I_c using Eq. (25) for each ϕ_0, we set the current at $I=1.05 I_c$, i.e., near the threshold. In the simulations of the infinite film, we have

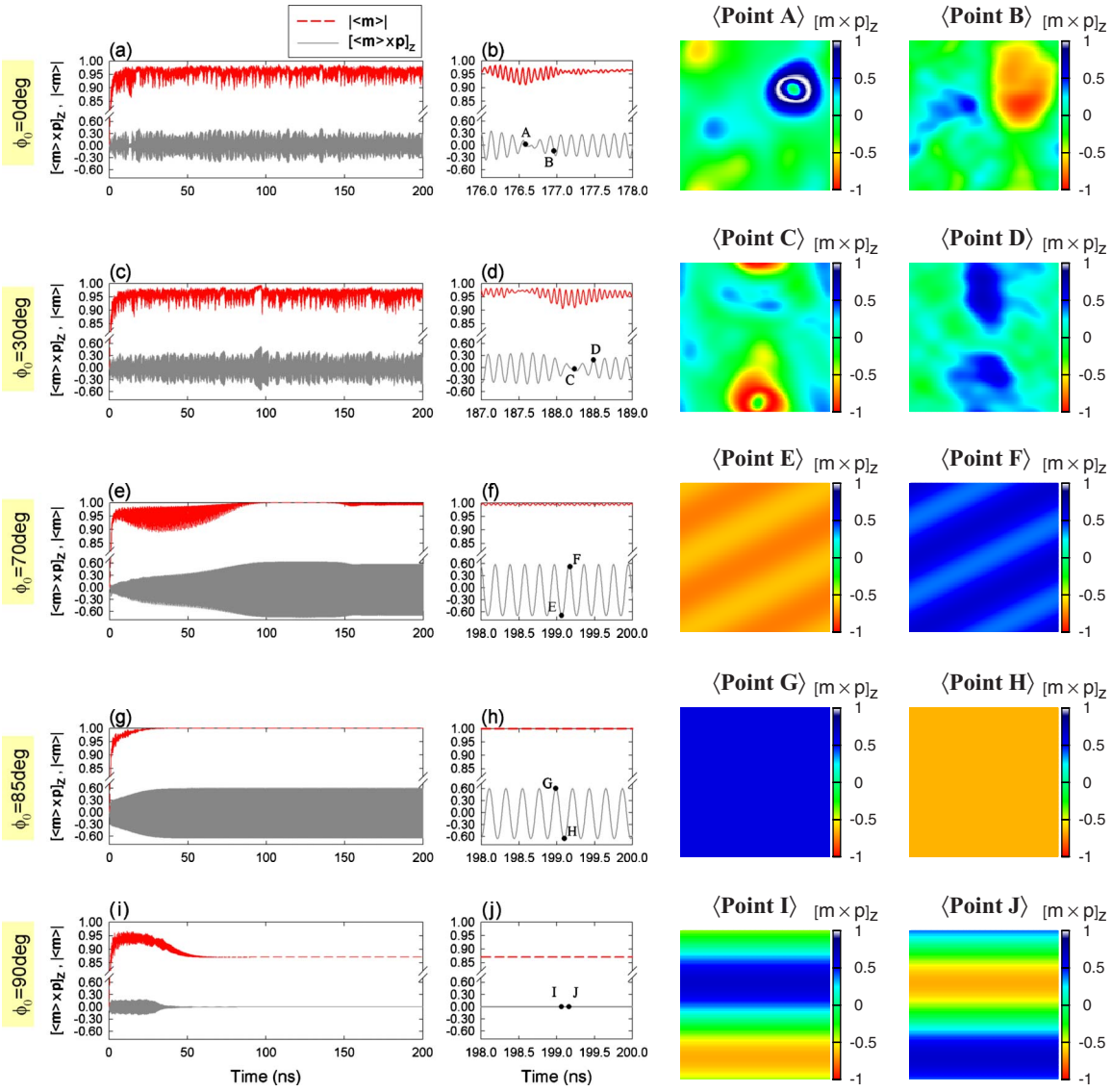

FIG. 4. (Color online) (first column) Time evolution of $|\langle \boldsymbol{m} \rangle|$ and $[\langle \boldsymbol{m} \rangle \times \boldsymbol{p}]_z$ in the infinite film, (second column) the shorter time scale plots of $|\langle \boldsymbol{m} \rangle|$ and $[\langle \boldsymbol{m} \rangle \times \boldsymbol{p}]_z$, and (third and fourth columns) the snapshots of magnetization-oscillation patterns $[\boldsymbol{m}(\boldsymbol{r},t) \times \boldsymbol{p}]_z$ at the points indicated by the capital letters for the in-plane field angles $\phi_0 = 0°$, 30°, 70°, 85°, and 90° as indicated on the left.

found that the calculated values of I_c approximately coincide with the simulated values. On the other hand, in the simulations of the elliptical film, we have found that the calculated values of I_c are a few percent larger than the simulated values. This is because the equilibrium state in the elliptical film obtained by the simulations is the spatially inhomogeneous state with the smaller threshold current.

We have numerically checked that the possible magnetization-oscillation patterns near the threshold do not depend on the direction of the pinned-layer vector $\boldsymbol{p}$ as long as the vector $\boldsymbol{p}$ satisfies $|\tan \beta_{eq}| \lesssim 1$. The simulation results shown below represent the near-threshold behavior of the magnetization dynamics for the pinned-layer magnetization vector $\boldsymbol{p}$ in the range of $|\tan \beta_{eq}| \lesssim 1$.

B. Infinite film

In this section, the dependence of magnetization dynamics on the in-plane field angle ϕ_0 in the infinite film is shown. We introduce the quantity $[\langle \boldsymbol{m} \rangle \times \boldsymbol{p}]_z$ to show the oscillation behavior, where the symbol $\langle \boldsymbol{m} \rangle$ denotes the average magnetization vector defined as

$$\langle \boldsymbol{m} \rangle = \frac{1}{\#\text{cells}} \sum_{j \in \text{cells}} \boldsymbol{m}(j). \tag{26}$$

We also introduce the length of the average magnetization vector $|\langle \boldsymbol{m} \rangle|$. This quantity gives the spatial uniformity degree; if $|\langle \boldsymbol{m} \rangle| = 1$, then the magnetization oscillation is completely uniform, and if $|\langle \boldsymbol{m} \rangle| = 0$, then the magnetization vectors are completely disordered. Since we use random initial conditions, the uniformity degree $|\langle \boldsymbol{m} \rangle|$ is approximately equal to zero at the initial time $t = 0$.

Figure 4 shows the time evolution of $|\langle \boldsymbol{m} \rangle|$ and $[\langle \boldsymbol{m} \rangle \times \boldsymbol{p}]_z$, the shorter time scale (the interval of 2 ns) plots of $|\langle \boldsymbol{m} \rangle|$ and $[\langle \boldsymbol{m} \rangle \times \boldsymbol{p}]_z$, and the snapshots of spatial patterns $[\boldsymbol{m}(x,y,t) \times \boldsymbol{p}]_z$ for the in-plane field angles $\phi_0 = 0°$, 30°, 70°,

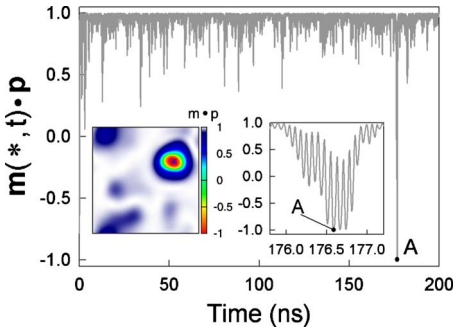

FIG. 5. (Color online) Main panel: time evolution of the $\boldsymbol{p}$ component of the magnetization vector located at the spatial point labeled with the asterisk symbol $(*)$ for $\phi_0=0°$. Inset: (left) snapshot of magnetization-oscillation pattern $\boldsymbol{m}(\boldsymbol{r})\cdot\boldsymbol{p}$ at the point A. The asterisk symbol $(*)$ denotes the spatial point which is paid attention. (Right) Enlargement of the interval between $t=175.5$ and 177.5 ns.

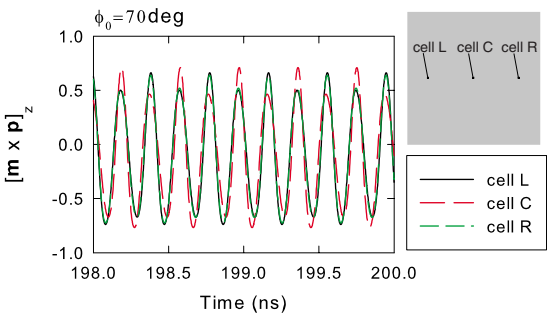

FIG. 6. (Color online) Time evolution of $[\boldsymbol{m}\times\boldsymbol{p}]_z$ for the spatial points of cell L, cell C, and cell R. The in-plane field angle is chosen as $\phi_0=70°$.

85°, and 90°. The currents of $\sigma I/2\pi=315.1$, 310.7, 292.0, 284.4, and 283.6 MHz are injected for $\phi_0=0°$, 30°, 70°, 85°, and 90°, respectively.

The propagating plane waves involving a uniform oscillation are observed for $\phi_0=85°$ and 90°. For $\phi_0=85°$, the uniform oscillation with $|\langle\boldsymbol{m}\rangle|=1$, in which all the magnetic moments oscillate in phase with the same amplitudes, is obtained in the steady state [Figs. 4(g) and 4(h)]. For $\phi_0=90°$, the propagating plane-wave pattern as well as the uniform-oscillation pattern emerges. Which types of pattern emerge depends on initial conditions, i.e., it depends on the choice of seeds for uniform pseudorandom numbers. In Figs. 4(i) and 4(j), the propagating plane-wave pattern is shown. The propagating plane wave can be interpreted as a synchronized state; all the local frequencies of the magnetic moments are the same and the phase differences between the magnetic moments are locked. Note that the propagating plane-wave pattern obtained has the wavelength of 500 nm (see the snapshots for the points I and J), which indicates that the plane-wave pattern is affected by the periodic boundary condition. In order to discuss the property of the propagating plane wave, it is probably necessary to perform the simulation on a much larger film but it is beyond the scope of the present paper. What is important now is that the coherent-oscillation pattern, in which all the local frequencies of magnetic moments are the same, emerges when $\phi_0\gtrsim 80°$. In particular, the completely uniform-oscillation pattern can emerge for $\phi_0\gtrsim 80°$.

In contrast to the coherent oscillation obtained for $\phi_0=85°$ and 90°, the incoherent oscillation, in which the amplitude and the phase are strongly disturbed, is observed for $\phi_0=0°$ and 30° [Figs. 4(a)–4(d)]. The uniformity degree $|\langle\boldsymbol{m}\rangle|$ randomly oscillates reflecting the strong amplitude and phase turbulence, and the large-amplitude, spatially localized events (see the snapshots for the points A and C) occur intermittently in space and time. The size of the localized region is about 100 nm. Figure 5 shows the time evolution of the $\boldsymbol{p}$ component of the magnetization vector located at the spatial point labeled with the asterisk symbol $(*)$ for $\phi_0=0°$. The point A shown in Fig. 5 denotes the same time as that shown in Fig. 4(b). The spatial pattern of $\boldsymbol{m}\cdot\boldsymbol{p}$ [the inset of Fig. 5] indicates that the oscillation amplitude in the localized region is very large. This large-amplitude oscillation appears and disappears within a few hundred picosecond as can be seen from the time evolution of $\boldsymbol{m}(*,t)\cdot\boldsymbol{p}$ [the inset of Fig. 5]. We believe that the large-amplitude, spatially localized, intermittent event corresponds to the CGL *burst* that is observed in the CGLE with the parameters of $c_{1,3}\ll -1$.[28,29]

In Figs. 4(e) and 4(f), the magnetization dynamics for $\phi_0=70°$ is shown. The behavior is the typical one obtained for $50°\lesssim\phi_0\lesssim 80°$. In this region of in-plane field angles, the weakly disturbed stripe pattern is observed in the steady state; the magnetization vectors oscillate regularly but small amplitude and phase fluctuations are seen. In Fig. 6, the time evolution of $[\boldsymbol{m}\times\boldsymbol{p}]_z$ for the spatial points of "cell L," "cell C," and "cell R" is shown. From Fig. 6, one can see that the small amplitude and phase fluctuations occur.

From the simulation results shown above, it is recognized that the transition from the incoherent to the coherent oscillation occurs at $\phi_0\sim 80°$. This is consistent with the theoretical prediction described in Sec. II B. Moreover, the large-amplitude, spatially localized, intermittent event such as the CGL burst has been observed for small in-plane field angles $(\phi_0\lesssim 30°)$. These results indicate that the CGLE, which is approximately derived from the LLGS equation, provides a qualitatively correct description of the collective magnetization dynamics excited by spin torque. Consequently, the magnetic film under spin torque can be treated as the oscillatory medium that is well described by the CGLE.

We comment on the relation between the spatially localized intermittent event and the self-localized spin-wave bullet. The spatial profile of the large-amplitude, spatially localized region [the inset of Fig. 5] is similar to that of the self-localized spin-wave bullet which is excited in the in-plane-magnetized nanocontact device.[6,7] In addition, both the modes emerge under the negative frequency nonlinearity. Accordingly, the spin-wave bullet can be interpreted as the stabilized CGL burst, i.e., the nanocontact geometry plays an essential role to stabilize the large-amplitude, spatially localized events.

In the nanocontact geometry, the propagating spin-wave mode has been observed when the out-of-plane field is applied to the film.[7,9] For the out-of-plane field, the nonlinear frequency shift is positive.[16] The propagating spin-wave mode observed in such a normally magnetized nanocontact is considered to be related to the coherent-oscillation mode

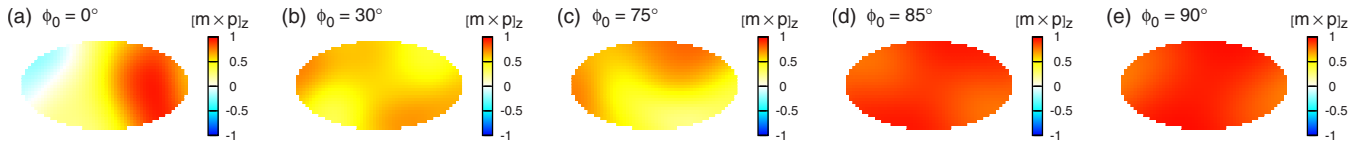

FIG. 7. (Color online) Representative snapshots of oscillation magnetization pattern in the elliptical magnetic film. The dependence on the in-plane field angle ϕ_0 is shown; ϕ_0=(a) 0°, (b) 30°, (c) 75°, (d) 85°, and (e) 90°.

we have obtained for ϕ_0=85° and 90°. The common ground of the two modes is that they are the synchronized states and that they emerge under the positive frequency nonlinearity. Based on the analogies between the two modes, we expect that the propagating spin-wave mode can emerge in the in-plane-magnetized nanocontact device composed of an in-plane anisotropic magnetic film when the in-plane field is applied along the hard axis.

C. Elliptical film

The dependence of magnetization dynamics on the in-plane field angle ϕ_0 in the elliptical film is shown in this section. Figure 7 depicts the representative snapshots of oscillation magnetization pattern $[\boldsymbol{m}(x,y)\times\boldsymbol{p}]_z$ for ϕ_0=0°, 30°, 75°, 85°, and 90°. These are the snapshots at the time that $[\langle\boldsymbol{m}\rangle\times\boldsymbol{p}]_z$ has a maximum value in the oscillation period. The currents of $\sigma I/2\pi$=315.1, 310.7, 289.1, 284.4, and 283.6 MHz are injected for ϕ_0=0°, 30°, 75°, 85°, and 90°, respectively. The simulation shows that the transition from the incoherent to the in-phase oscillation occurs at $\phi_0\sim$80°. For ϕ_0=0°, 30°, and 75°, the incoherent oscillations emerge. On the other hand, for ϕ_0=85° and 90°, the almost uniform, in-phase oscillations emerge. The incoherent oscillations are classified into two types: a strongly disturbed oscillation for ϕ_0=0° and a weakly disturbed oscillation for ϕ_0=30° and 75°. For ϕ_0=0°, 75°, and 90°, we show the time evolution of $|\langle\boldsymbol{m}\rangle|$ and $[\langle\boldsymbol{m}\rangle\times\boldsymbol{p}]_z$ in Fig. 8, and the time evolution of $[\boldsymbol{m}\times\boldsymbol{p}]_z$ for the spatial points of cell L, cell C, and cell R in Fig. 9.

In the case of ϕ_0=90°, an almost uniform in-phase oscillation emerges in the steady state. The uniformity degree is approximately one ($|\langle\boldsymbol{m}\rangle|\simeq 1$) [Fig. 8(e)], and all the magnetization vectors oscillate in phase accompanying small amplitude fluctuations [Fig. 9(c)]. This in-phase oscillation corresponds to the synchronized oscillation patterns obtained in the infinite film for $\phi_0\gtrsim$80° presented in the previous section. The origin of the amplitude fluctuations is probably the inhomogeneous distribution of the demagnetizing field due to the effect of elliptical shape.

In the case of ϕ_0=75°, small amplitude and phase fluctuations occur [Fig. 9(b)], and the weakly disordered pattern emerges. The oscillation behavior shown in Fig. 9(b) is similar to that shown in Fig. 6. The pattern shown in Fig. 7(b) or 7(c) is therefore analogous to the weakly disturbed behavior observed in the infinite film.

In the case of ϕ_0=0°, the amplitude as well as the phase is disturbed [Fig. 9(a)], and the strongly disordered pattern emerges [Fig. 7(a)]. The pattern shown in Fig. 7(a) is analogous to the strongly disturbed behavior observed in the infinite film because a large-amplitude, spatially localized region is seen at the right side of the ellipse. Unlike the case of the infinite film, the large-amplitude region appears with regular rhythm [Figs. 8(a) and 8(b)]. This is probably due to the effect of elliptical boundaries.

In Fig. 10, the oscillation behavior for ϕ_0=0° just above the onset of the oscillation threshold is shown. The magni-

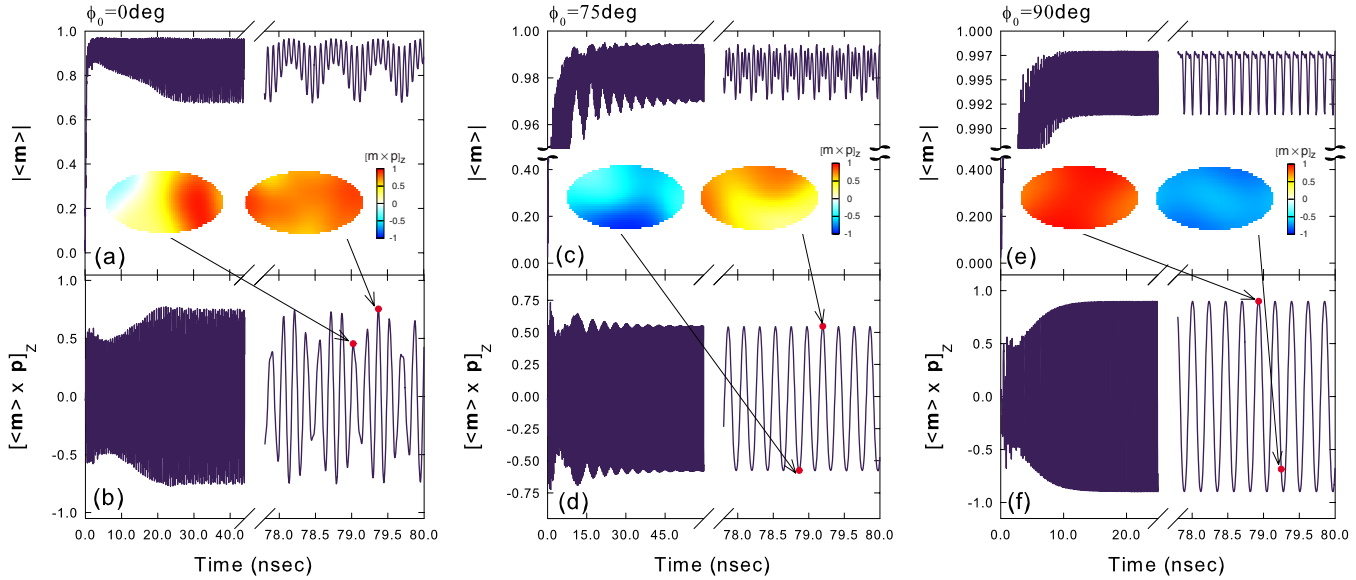

FIG. 8. (Color online) Time evolution of $|\langle\boldsymbol{m}\rangle|$ and $[\langle\boldsymbol{m}\rangle\times\boldsymbol{p}]_z$, and the snapshots of magnetization-oscillation patterns $[\boldsymbol{m}(x,y,t)\times\boldsymbol{p}]_z$ at the time labeled by the dots in the elliptical film for ϕ_0=0°, 75°, and 90°.

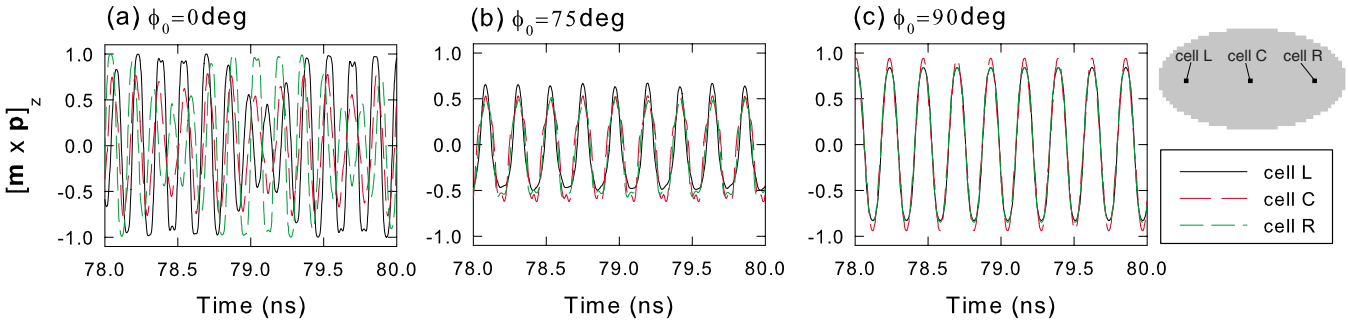

FIG. 9. (Color online) Time evolution of $[\boldsymbol{m}\times\boldsymbol{p}]_z$ for the spatial points of cell L, cell C, and cell R. The in-plane field angles are ϕ_0 =(a) 0°, (b)75°, and (c)90°.

tude of the current is chosen as σI=294.1 MHz. In this low-current regime, the oscillation state is seemingly homogeneous since $|\langle \boldsymbol{m}\rangle| \simeq 0.99$ [Fig. 10(a)]. However, the amplitude as well as the phase is strongly disturbed [Fig. 10(b)], which is similar to the behavior shown in Fig. 9(a). The spatial uniformity of $|\langle \boldsymbol{m}\rangle| \simeq 0.99$ results just from the smallness of the oscillation amplitude due to the small magnitude of the current. The property of the oscillation for σI =294.1 MHz [Fig. 10] is essentially the same as that for σI=315.1 MHz [Figs. 8(a), 8(b), and 9(a)]. A magnetization-oscillation pattern similar to that shown in Fig. 10 has been reported in the several papers[30–32] (see, e.g., Fig. 2 in Ref. 30 and Fig. 1(b) in Ref. 31); such an oscillation emerges in the low-current regime under the bias field with small angle ϕ_0. Although the inhomogeneity of the oscillation is small ($|\langle \boldsymbol{m}\rangle| \simeq 1$), the magnetic moments do not oscillate in phase.

The simulation results for the elliptical film shown above are basically consistent with the simulation results in the infinite film shown in Sec. III B and the theoretical prediction described in Sec. II B, although the effect of elliptical boundaries on magnetization dynamics has been observed. This indicates that the transition from the incoherent to the in-phase oscillation obtained by the simulation for the elliptical film mainly originates from the cooperative effect between the exchange spin-wave dispersion and the nonlinear shift of local frequencies. In the experimental results reported by the authors of Refs. 11 and 12, the spectrum linewidth of the elliptical STO decreases as the in-plane bias field is rotated from the in-plane easy axis to the hard axis. We believe that the variation in the spectrum linewidth originates from the spatial coherence of the free-layer magnetization dynamics dominated by the cooperative effect mentioned above.

The emergence of in-phase oscillations in the elliptical film suggests that the single-domain (macrospin) approximation is applicable to the fairly large element with the size of 130×70 nm^2 if an in-phase oscillation emerges. This is in contrast with the widely accepted consequence of micromagnetics that the single-domain approximation is valid when the size of the element is smaller than $4-8\times l_{\mathrm{ex}}(\simeq 40$ nm) [33] but because the uniformity of the magnetization oscillation is the dynamical uniformity, not the static one, there are no inconsistencies.

IV. CONCLUSION

On the basis of the CGLE for the spin-torque-induced excitations, it is expected that some synchronized states can emerge in magnetic pillar structures when the nonlinear frequency shift is positive. For the in-plane-magnetized, anisotropic, thin films, this can be achieved when a bias field is applied along the direction far from the in-plane easy axis. We have confirmed the theoretical prediction by the micromagnetic simulations. The simulations have been performed on two kinds of magnetic films: the infinite film and the elliptical film. The simulation for the infinite film has been performed in order to mediate between the simulation for the elliptical film and the theory based on the CGLE. In the simulation for the elliptical film, we have demonstrated that the in-phase oscillation emerges under the bias field in the direction far from the in-plane easy axis in accordance with the theory based on the CGLE. The consistency between the theory and the simulations indicates that the spin-torque-induced dynamics near the oscillation threshold is signifi-

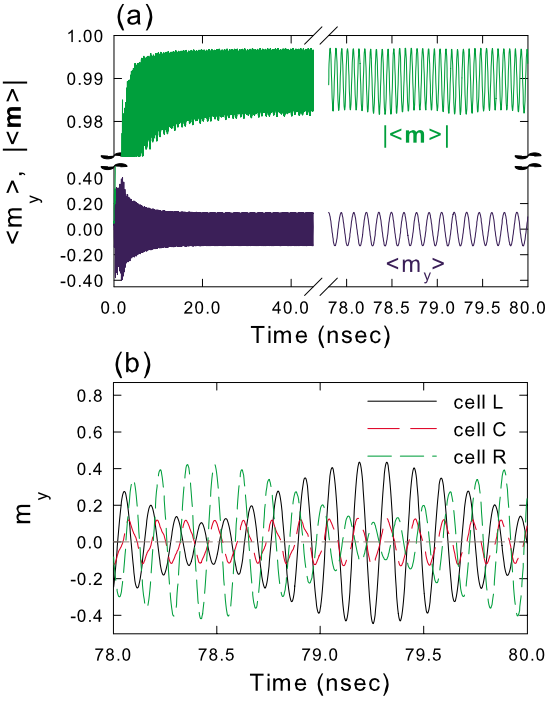

FIG. 10. (Color online) (a) Time evolution of $\langle m_y\rangle$ and $|\langle \boldsymbol{m}\rangle|$ for ϕ_0=0° in the elliptical film just above the onset of the oscillation threshold. (b) Time evolution of m_y for the spatial points of cell L, cell C, and cell R. The magnitude of the current is chosen as σI =294.1 MHz.

cantly influenced by the cooperative effect between the exchange spin-wave dispersion and the nonlinear shift of local frequencies, and that the positive frequency nonlinearity is necessary for the emergence of the in-phase oscillation in the elliptical nanopillar device.

ACKNOWLEDGMENTS

K.K. would like to thank Hirofumi Morise for useful discussion on the LLGS dynamics and micromagnetic simulations.

*kiwamu.kudo@toshiba.co.jp

[1] S. I. Kiselev, J. C. Sankey, I. N. Krivorotov, N. C. Emley, A. G. F. Garcia, R. J. Schoelkopt, R. A. Buhrman, and D. C. Ralph, Nature (London) **425**, 380 (2003).

[2] W. H. Rippard, M. R. Pufall, S. Kaka, S. E. Russek, and T. J. Silva, Phys. Rev. Lett. **92**, 027201 (2004).

[3] J. A. Katine and E. E. Fullerton, J. Magn. Magn. Mater. **320**, 1217 (2008).

[4] T. J. Silva and W. H. Rippard, J. Magn. Magn. Mater. **320**, 1260 (2008).

[5] J. C. Slonczewski, J. Magn. Magn. Mater. **195**, 261 (1999).

[6] A. N. Slavin and V. Tiberkevich, Phys. Rev. Lett. **95**, 237201 (2005).

[7] G. Consolo, B. Azzerboni, G. Gerhart, G. A. Melkov, V. S. Tiberkevich, and A. N. Slavin, Phys. Rev. B **76**, 144410 (2007).

[8] D. V. Berkov and N. L. Gorn, Phys. Rev. B **76**, 144414 (2007).

[9] S. Bonetti, V. Tiberkevich, G. Consolo, G. Finocchio, P. Muduli, F. Mancoff, A. Slavin, and J. Åkerman, arXiv:0909.3331 (unpublished).

[10] A. M. Deac, A. Fukushima, H. Kubota, H. Maehara, Y. Suzuki, S. Yuasa, Y. Nagamine, K. Tsunekawa, D. D. Djayaprawira, and N. Watanabe, Nat. Phys. **4**, 803 (2008).

[11] K. V. Thadani, G. Finocchio, Z.-P. Li, O. Ozatay, J. C. Sankey, I. N. Krivorotov, Y.-T. Cui, R. A. Buhrman, and D. C. Ralph, Phys. Rev. B **78**, 024409 (2008).

[12] T. Wada, T. Yamane, T. Seki, T. Nozaki, Y. Suzuki, H. Kubota, A. Fukushima, S. Yuasa, H. Maehara, Y. Nagamine, K. Tsunekawa, D. D. Dyayaprawira, and N. Watanabe, J. Magn. Soc. Jpn. **33**, 379 (2009).

[13] D. Berkov and N. Gorn, Phys. Rev. B **71**, 052403 (2005).

[14] A. N. Slavin and V. Tiberkevich, IEEE Trans. Magn. **44**, 1916 (2008).

[15] I. S. Aranson and L. Kramer, Rev. Mod. Phys. **74**, 99 (2002).

[16] A. N. Slavin and P. Kabos, IEEE Trans. Magn. **41**, 1264 (2005).

[17] V. Tiberkevich, I. Krivorotov, G. Gerhart, and A. Slavin, J. Magn. Magn. Mater. **321**, L53 (2009).

[18] K. Kudo, T. Nagasawa, R. Sato, and K. Mizushima, J. Appl. Phys. **105**, 07D105 (2009).

[19] K. Mizushima, T. Nagasawa, K. Kudo, Y. Saito, and R. Sato, Appl. Phys. Lett. **94**, 152501 (2009).

[20] K. Kudo, T. Nagasawa, R. Sato, and K. Mizushima, Appl. Phys. Lett. **95**, 022507 (2009).

[21] A. Pikovsky, M. Rosenblum, and J. Kurths, *Synchronization: A Universal Concept in Nonlinear Dynamics* (Cambridge University Press, Cambridge, England, 2001).

[22] G. Gerhart, E. Bankowski, G. A. Melkov, V. S. Tiberkevich, and A. N. Slavin, Phys. Rev. B **76**, 024437 (2007).

[23] Y. Kuramoto and T. Tsuzuki, Prog. Theor. Phys. **52**, 1399 (1974).

[24] Y. Kuramoto, *Chemical Oscillation, Waves, and Turbulence* (Dover, New York, 2003).

[25] H. Mori and Y. Kuramoto, *Dissipative Structures and Chaos* (Springer, Berlin, 1998).

[26] J. C. Slonczewski, J. Magn. Magn. Mater. **159**, L1 (1996).

[27] N. Hayashi, K. Saito, and Y. Nakatani, Jpn. J. Appl. Phys., Part 1 **35**, 6065 (1996).

[28] J.-W. Kim and E. Ott, Phys. Rev. E **67**, 026203 (2003).

[29] V. Nagy and E. Ott, Phys. Rev. E **76**, 066206 (2007).

[30] X. Zhu, J.-G. Zhu, and R. M. White, J. Appl. Phys. **95**, 6630 (2004).

[31] D. V. Berkov and N. L. Gorn, Phys. Rev. B **72**, 094401 (2005).

[32] I. N. Krivorotov, D. V. Berkov, N. L. Gorn, N. C. Emley, J. C. Sankey, D. C. Ralph, and R. A. Buhrman, Phys. Rev. B **76**, 024418 (2007).

[33] A. Hubert and R. Schäfer, *Magnetic Domains* (Springer, Berlin, 1998).